Supporting information for

Hydrogen Bond-Mediated pH-Universal Electrocatalytic Hydrogen Production by Conjugated Porous Poly-Indigo

Ipsita Nath,[a,b] Jeet Chakraborty,[a,b,*] Reinaud Lips,[a,c] Sander Dekyvere,[a] Jiang Min,[a] Rajender S. Varma,[d] and Francis Verpoort[a,e,*]

[a]Laboratory of Organometallics, Catalysis and Ordered Materials, State Key Laboratory of Advanced Technology for Materials Synthesis and Processing, Center for Chemical and Material Engineering, Wuhan University of Technology, Wuhan 430070, P.R. China.

[b]Department of Chemistry, Ghent University, Krijgslaan 281, Ghent, Belgium, 9000.

[c]Odisee Technologiecampus Gent, Ghent, Belgium, 9000.

[d]Regional Centre of Advanced Technologies and Materials, Czech Advanced Technology and Research Institute, Palacký University in Olomouc, Šlechtitelů 27, 783 71 Olomouc, Czech Republic.

[e]National Research Tomsk Polytechnic University, Lenin Avenue 30, Tomsk 634050, Russia.

*Correspondence:

jeet.chakraborty@hotmail.com (J.C.)

francis@whut.edu.cn (F.V.)

Materials:

The chemicals and solvents (AR grade) used for Ind-CPP synthesis were obtained from Aladdin China and used without further purifications.

Characterization: ^{13}C-CP/MAS NMR spectra analyses were measured on a Bruker Advance 400 DSX spectrometer. Cross Polarization Magic Angle Spinning (CP/MAS) was performed at MAS of 10 kHz in a 4 mm zirconia rotor. TPPM decoupling was used for acquisition. FTIRs were recorded on a Bruker Vertex 80V. The morphology was determined by an S4800 field emission scanning electron microscope (FESEM, Hitachi, Japan). TEM analysis was carried out in a Philips CM20 microscope at 200 kV. Imaging and diffraction of the structure were performed at a low electron dose for minimizing beam damage to the sample. SEAD pattern was collected using the same CM20 instrument. The binding energies of the elements present in the polymer were measured by XPS on Thermo Fisher ESCALAB 250Xi. Powder XRD analyses were performed on Bruker D8 Advance diffractometer with a copper Kα radiation source (λ= 1.54056 Å) at 40 kV and 45 Ma with 5 °/sec scanning speed. UV-vis absorption spectra were recorded in the solution phase on Shimadzu UV-1800 UV-visible spectrophotometer using a 10 mm path length quartz cuvette. The materials in the respective solvents were sonicated for 10 min to ensure complete dissolution before measurement. The cyclic voltammograms and EIS were investigated on a CHI-660E workstation using a typical three-electrode system. 0.1 M NBu$_4$PF$_6$ in acetonitrile was used as the electrolyte for the CV analysis using Ag/AgNO$_3$ as the reference electrode, whereas 0.5 M aqueous H$_2$SO$_4$, 1M aqueous KOH, and phosphate buffer solution (pH 7) were used for EIS measurements against Ag/AgCl (3M KCl) as the reference electrode. These results were then converted to RHE electrode.

Notes:

1) Due to the presence of strong H-bond donating and accepting sites, Ind-CPP strongly associates with a myriad of solvent molecules (possessing H-bond donating or accepting ability e.g., water, DMF, alcohols, acetone, etc.) as trapped guests. The synthesized material (following the process described before) was, therefore, dried at 100 °C in vacuum for 12 h before subjecting to the solid-state NMR analysis. This ensured that no organic solvents remained trapped inside the material, which may interfere with the NMR output.

2) Alike solid-state NMR, the sample was prepared in a similar manner for IR analysis to nullify any contribution from trapped solvents (including H$_2$O). That's also the very reason we opted for ATR-FTIR instead of the conventional one because ATR-FTIR analysis doesn't require prior palate preparation minimizing aerial exposure, and *ipso facto*, chances to absorb atmospheric moisture.

4. Experimental Section

4.1. Synthesis of Ind-CPP: In a typical synthesis, a schlenk flask equipped with a medium-sized magnetic spinner was charged with Tyrian purple (126 mg), and 1,3,5-triethynylbenzene (30 mg) in a glovebox under Ar-atmosphere. 50 mL of dry activated DMF and 10 mL of activated triethylamine are added to this mixture, sealed, and sonicated for 15 min to bring the mixture to a homogeneous suspension. $Pd(PPh_3)_4$ (10 mg) was then added and the reaction mixture was gradually heated to 120 °C over a period of 1 h with rigorous stirring (800 rpm). The reaction was continued at 120 °C for 6 days maintaining the inert atmosphere. After 3 days, dark bottle green-coloured precipitate, visible to the naked eye, starts appearing throughout the reaction bulk, and the amount of CPP intensified on further prolonging the reaction for 3 more days. After completion of the reaction, the solid product is collected through repeated centrifugation and the ensuing compound was washed with DMF until the supernatant liquid becomes colourless, followed by rinsing with methanol, acetone, and dichloromethane. The collected product was further purified in a Soxhlet extractor using dichloromethane as the solvent to ensure the removal of any residual solvent trapped in the polymer through H-bonding After drying in a vacuum oven at 80 °C for 12h, the final compound was collected as a dark green amorphous powder.

4.2. Electrochemical HER: The electrochemical HER was performed in a standard three-electrode system in an undivided electrolyser using Ind-CPP drop cast on a glassy carbon electrode as the working electrode, carbon paper as the counter electrode, and Ag/AgCl (3M KCl) as the reference electrode in 0.1 M $H_2 SO_4$ aq., 1 M KOH aq., and PBS aq. (pH 7). The data obtained were converted to RHE electrodes using the formula:

$$E_{RHE} = E_{Ag/AgCl} + 0.0591 \times pH + 0.197$$

The CPP ink was prepared by dispersing 2 mg of the material in 500 µL isopropanol/water (3:2 v/v) mixture using Nafion (50 µL) as the binder. 15 µL of the ink was drop cast on a freshly polished glassy carbon electrode (surface area 0.0707 cm^2) and air-dried to prepare the working electrode. The electrolyte was degassed by purging ultrapure N_2 for 15 min, and the electrode was dipped in respective solutions for 30 min before subjecting to catalysis to ensure equal catalyst-water contact at all sites, and zero aerial interference. The measurements were carried out on a CHI-660E workstation.

4.5. Material modelling: The material was modelled using Materials Studio and the geometry and energy were optimized using AM1 Hamiltonian with restricted Hartree-Fock in the VAMP module. The same module was used to optimize the structures of the catalytic intermediates (i.e., reduced CPP, its association with water, proton etc.) as well. The enthalpy of formation and zero-point energy values were used to assess the feasibility of the catalysis.
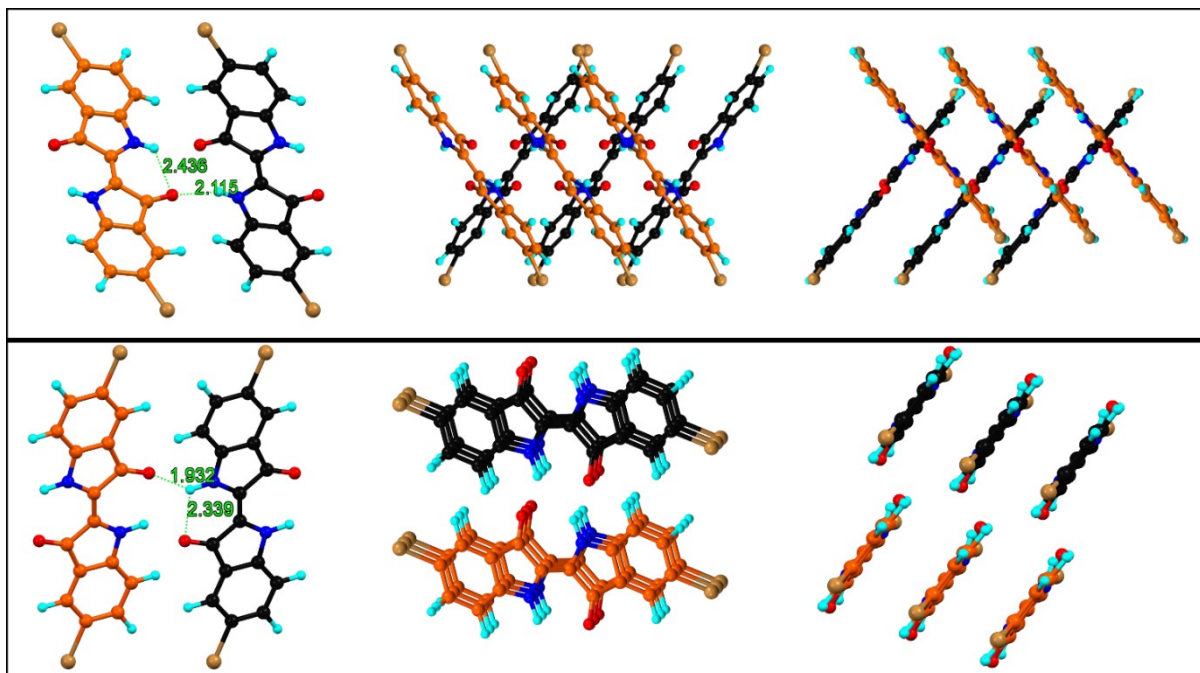
Fig. S1. Crystal structure of 6,6′-dibromoindigo (Tyrian Purple) featuring two different polymorphs: the bulk phase (top panel) and the surface-induced phase (bottom panel) viewed along different crystal axes. Colour scheme: cyan H; red O; blue N; brown Br, orange and black C. The C atoms of indigo from two adjacent crystal planes have been differently colour coated as black and orange for easy detection.

Discussion S1: Crystal structure of Tyrian Purple

The crystal structure of 6,6′-dibromoindigo (Tyrian Purple) is visualized from different axes. The molecule crystallizes in two different polymorphs: (surface-induced growth, and (ii) bulk growth.[1] The two adjacent layers of indigo are coloured in black and orange respectively for clear detection. In both polymorphs, intra and intermolecular H-bonding between the carbonyl O and the amine H can be perceived. Apart from this, intrinsic π–stacking exists between identical layers as well. Due to such intricate van der Waals' attractions (i.e., H-bonding and π–stacking), the self-aggregated molecular crystals become insoluble in most of the solvents and sparingly dissolves in extreme polar solvents e.g., DMF, DMSO or NMP. The length of the H-bonds present in the bay region of both crystals varies from each other. While the intramolecular H-bond length is *ca.* 2.4 Å, the inter-molecular (or inter planner) distance shrinks drastically in the surface-induced crystal.
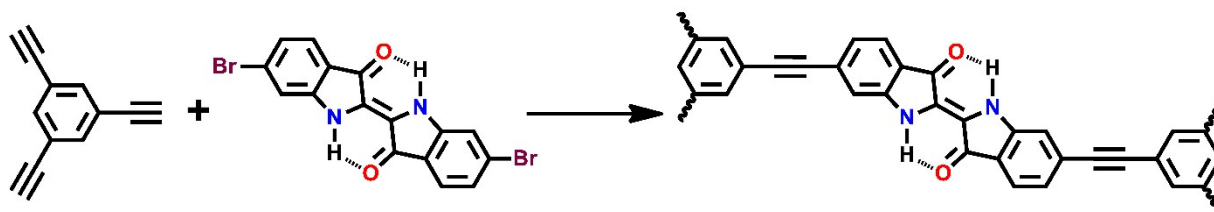
Fig. S2. Synthetic scheme for the preparation of Ind-CPP.

**Discussion S2: Synthetic considerations of Ind-CPP**

(i) Typically, the H-bond donating/accepting functionalities of a reactant are initially protected with auxiliary moieties, and after Sonogashira reaction, they are de-protected. Indigo is no exception in this regard. However, we reckon that protecting the amine ends would dissipate the H-bonding effect i.e., the Ind-reactants will become easily soluble in the reaction medium. While better solubility is indeed beneficial for efficient coupling, the resultant CPP may not acquire the targeted sheet-type morphology due to rapid kinetically driven polymerization. This may lead to poor or no exfoliation at all, effectively decreasing the dispersibility of the material and its water association sites (i.e., H-bonding sites) for HER.

(ii) We comprehend that to maintain effective catalytic activity, consideration (i) needs to be followed. However, the price for that may include (a) poor product yield due to inefficient reaction (constrained reactivity of Tyrian purple), and (b) rigorous synthetic condition. Therefore, a high 120 °C temperature was maintained for the CPP synthesis, and the reaction was carried on for 6 successive days with vigorous stirring (800 rpm). Visibly recognizable deep bottle-green coloured particles of Ind-CPP started to appear from *ca.* 60 h onwards during the polymerization. Continuing the reaction for another 3-day ensured maximum reactivity of the Tyrian purple.

(iii) Apart from these, we also assumed that the presence of Cu-salts (routinely used in Sonogashira coupling) may activate the terminal alkynes at high temperatures for a prolonged reaction span. Considering this, in addition to the restrained reactivity of Tyrian purple may lead to substantial homo-coupling of the terminal alkynes (Glaser coupling), thereby poisoning the desired CPP backbone. Hence, to deal with this situation, a Cu-free protocol was adopted instead.
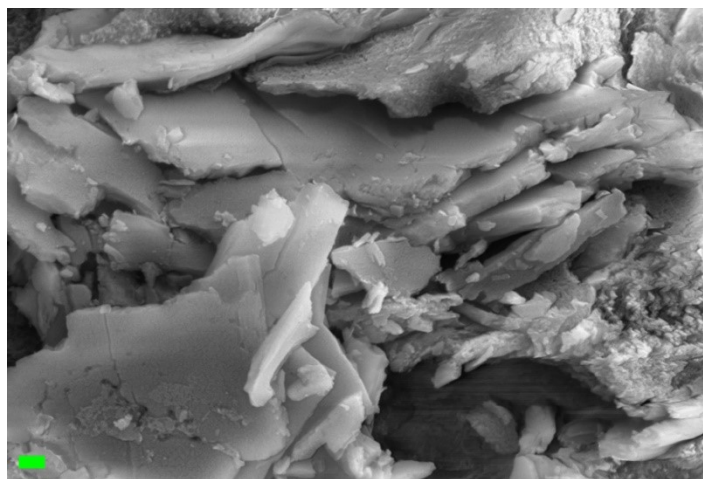
Fig. S3. FESEM image of Ind-CPP. Scale bar 200 nm.
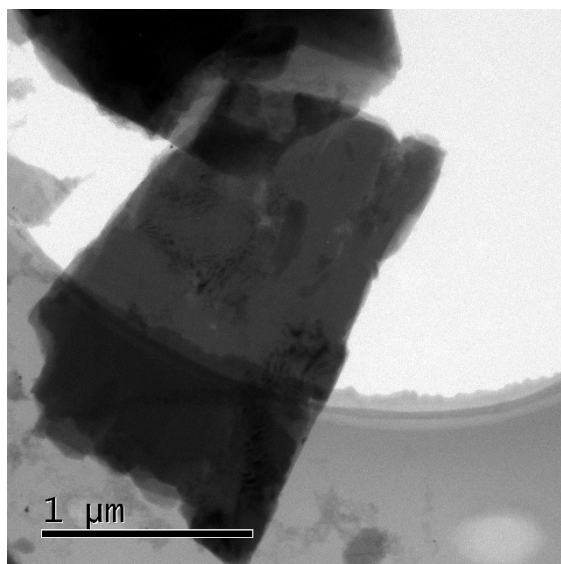
Fig. S4. TEM image of Ind-CPP.

Discussion S3: Morphology of Ind-CPP

The thickness of the as-synthesized CPP particles was observed to be *ca.* 200 nm from the FESEM image indicating multiple layers were stacked to generate a chunk. The TEM image, on the other hand, shows only a nominal thickness of the CPP. From the TEM image given in Fig. 1c (main text) only 6 CPP layers can be perceived, which is significantly lower than that displayed in the FESEM. The TEM image provided here also demonstrate only a nominal thickness. This observation conferred that the CPP layers were sonochemically exfoliated during sample preparation for TEM and generated few-layer CPPs. Such sonochemical exfoliation of 2D layered materials (e.g., graphene, MS_2 where M is transition metal, COFs, MXenes, etc.) into mono- or few-layers are whelming in literature.[2]
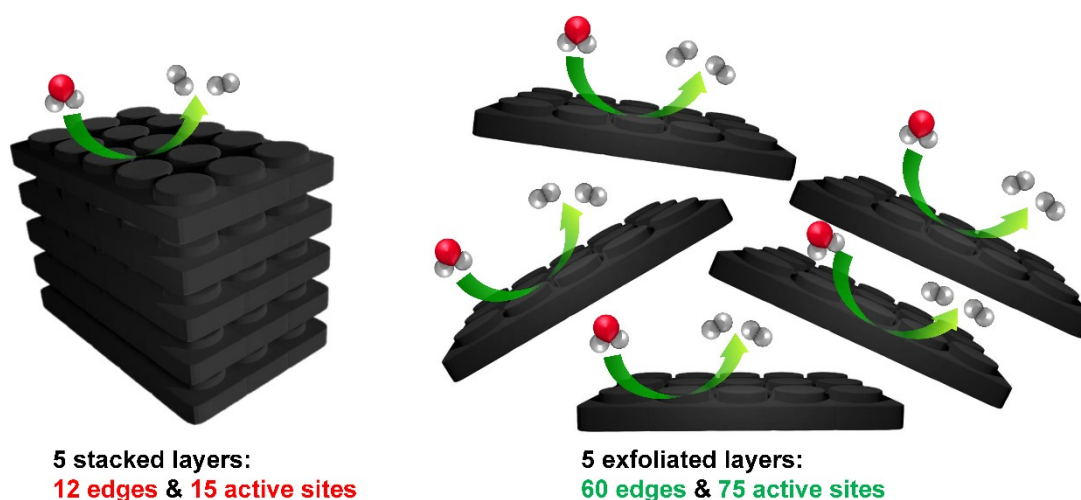
Fig. S5. Schematic illustration of the effect of exfoliation on HER compared to the bulk Ind-CPP.

Discussion S4: Effect of exfoliation on the catalytic activity of Ind-CPP

The plausible effect of exfoliation on the overall catalytic performance of Ind-CPP towards HER is depicted in a simple schematic and qualitative way. Deliberating the Ind-CPP layers as Lego plates with the studs as H-bonding sites, one can simply contemplate that for a bulk chunk, the studs of only the top plate will be available for H-bonding with water and serve as active catalytic sites for HER. Apart from the studs, the edges and vertices can also play the roles of active water-contact sites. The schematic illustration presented in the picture takes a cuboid chunk made of five 3×5 Lego plates as the bulk CPP simulator, which offers only 15 active H-bonding sites (i.e., 15 naked studs of the top plate), 8 vertices and 12 edges. Compared to that, when exfoliated into five individual plates, it offered 5 times higher active sites (i.e., 75 active H-bonding sites, 60 edges and 40 vertices). Evidently, the exfoliated material will manifest enhanced water associability, and *de facto* augmented HER propensity.

The experimental observation perceived from the FESEM and TEM analysis of Ind-CPP fueled the possibility of sonochemically exfoliated few-layer CPP generation, and better HER catalytic performance thereof.
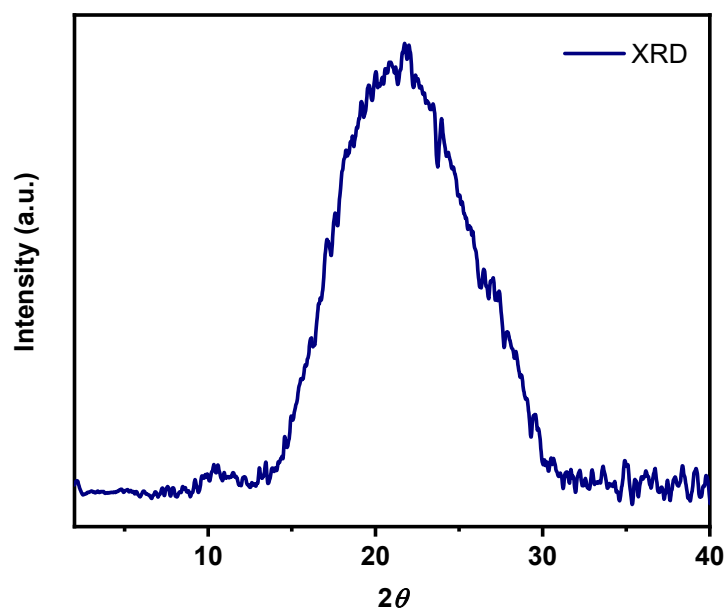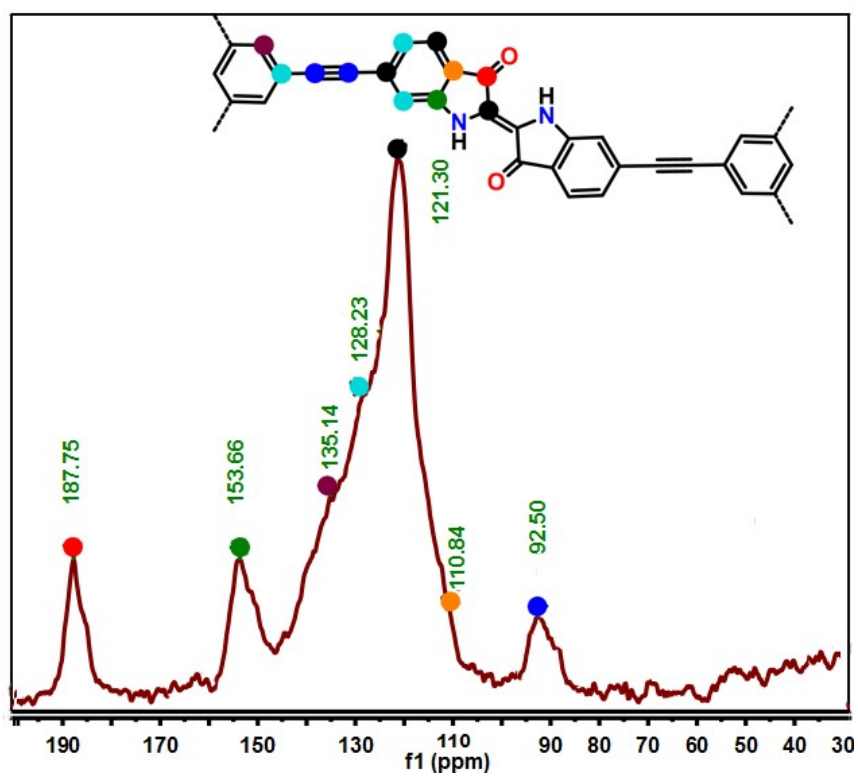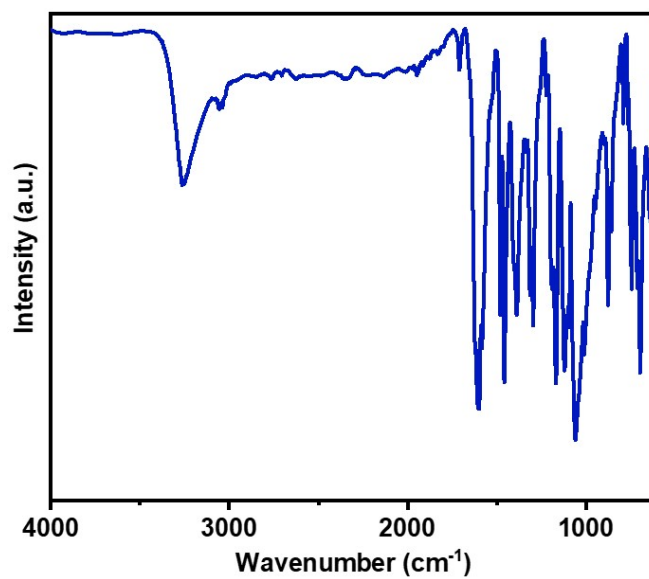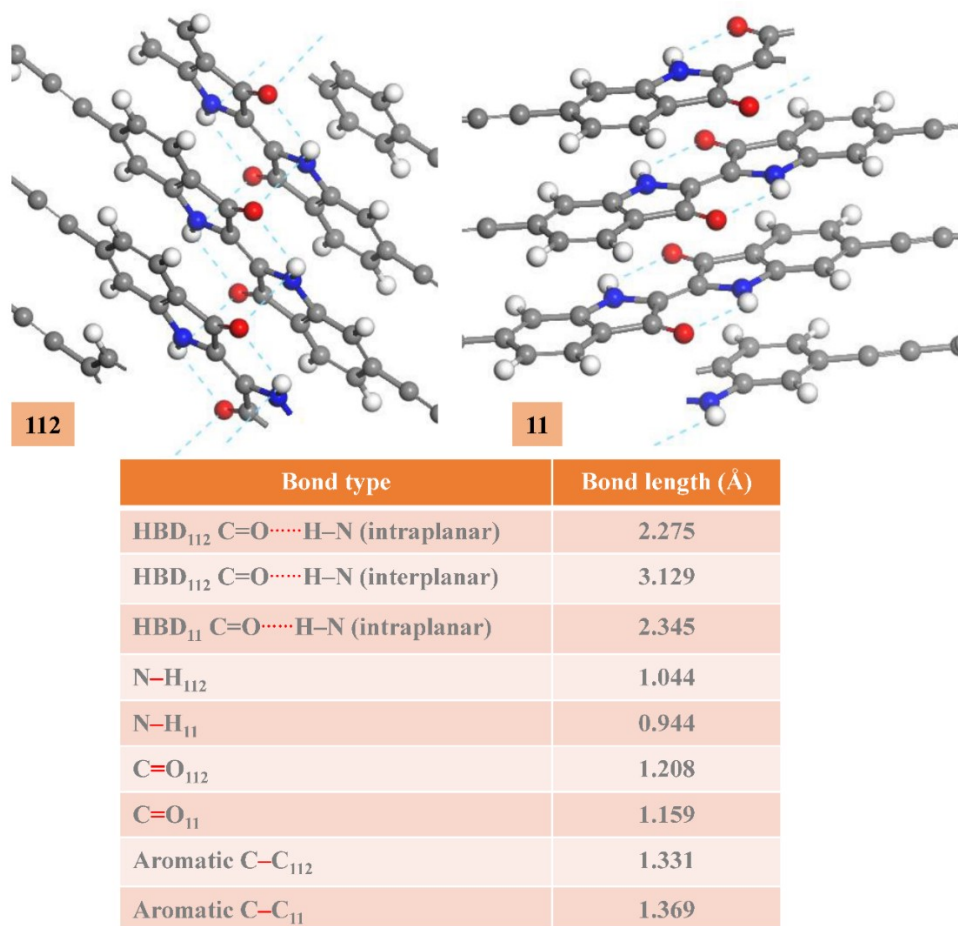
Fig. S6. XRD pattern of Ind-CPP.

Fig. S7. Solid-state ^{13}C-NMR spectrum of Ind-CPP with colour-coded signals for corresponding carbons.

Fig. S8. ATR-FTIR pattern of Ind-CPP.

Table S1. Characteristic IR peaks of Ind-CPP with due assignments.

Frequency (cm^{-1})	Peak assignment
3258	-N−H stretch
3050	Aromatic -C−H stretch
1700 and 1620	-C=O stretch
1600 and 1578	Aromatic -C=C- stretch of indigo

Bond type	Bond length (Å)
HBD$_{112}$ C=O⋯⋯H–N (intraplanar)	2.275
HBD$_{112}$ C=O⋯⋯H–N (interplanar)	3.129
HBD$_{11}$ C=O⋯⋯H–N (intraplanar)	2.345
N–H$_{112}$	1.044
N–H$_{11}$	0.944
C=O$_{112}$	1.208
C=O$_{11}$	1.159
Aromatic C–C$_{112}$	1.331
Aromatic C–C$_{11}$	1.369

Fig. S9. Computed geometry and energy-optimized structure of Ind-CPP showing HBD$_{112}$ (top left) and HBD$_{11}$ (top right) interactions. The bond lengths (red) of individual functional units are tabulated (bottom). Colour code: grey, C; white, H; blue, and N; red, O.

Discussion S5: FTIR

The -N–H, -C=O, and aromatic -C=C- stretch of indigo can be deconvoluted, which is provided in the main text (Fig. 1g). Hooke's law state that the IR frequency ω is related to the force constant k (which is directly proportional to the length of a particular bond) and mass μ as:

$$\omega = \frac{1}{2\pi c}\sqrt{\frac{k}{\mu}}$$

Where c is the speed of light. Evidently, $\omega \propto \sqrt{k}$ for a fixed μ. Considering the calculated bond lengths and H-bonding distances given in Fig. S8, the bond strength follows the order:

N–H$_{11}$ > N–H$_{112}$, C=O$_{11}$ > C=O$_{112}$, and Aromatic C=C$_{112}$ > C=C$_{11}$.

The deconvoluted FTIR pattern for these peaks followed this exact trend (Fig. 1g) providing experimental validation to this theoretical postulate.
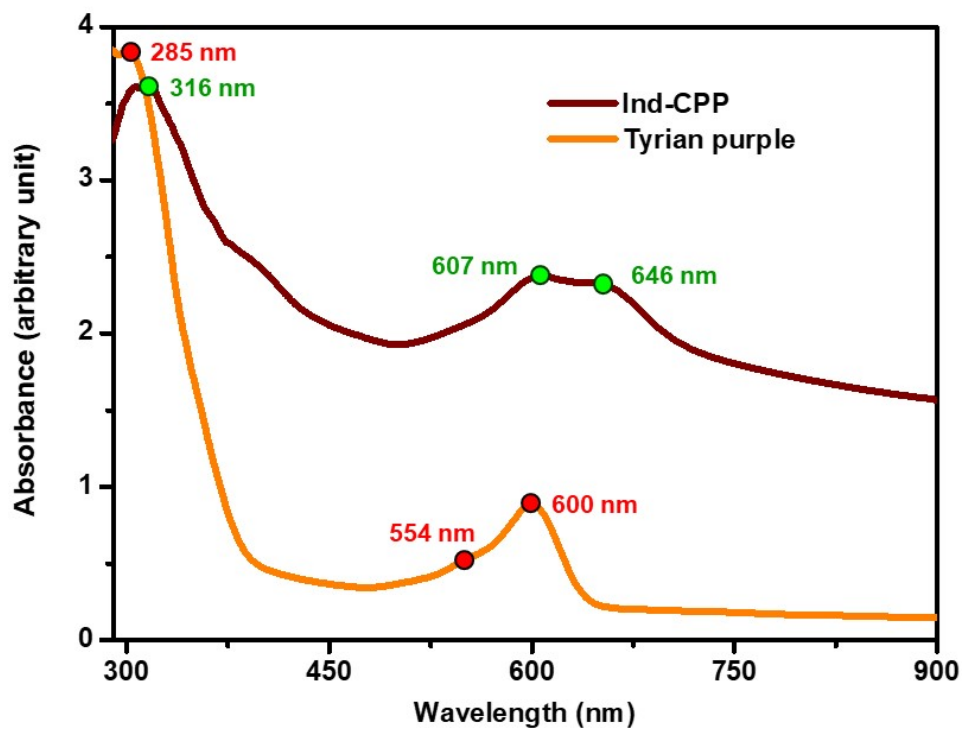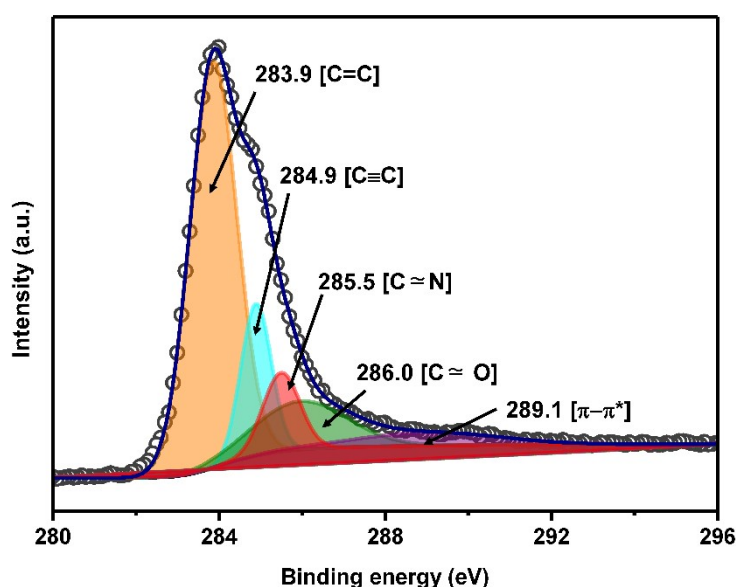
Fig. S10. UV-Vis absorption spectra of Ind-CPP (wine) and Tyrian Purple (Orange). The positions of the peaks are indicated to show their redshift after polymerization.
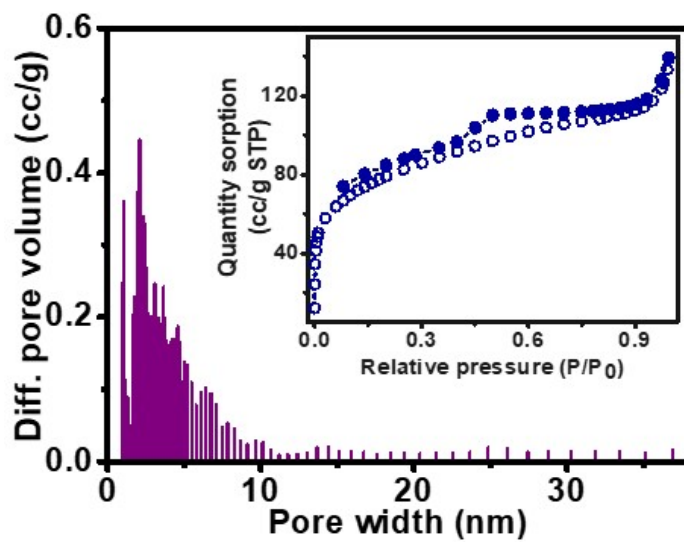
Fig. S11. NLDFT porosity pattern of Ind-CPP with its N_2 sorption isotherm plot (inset).
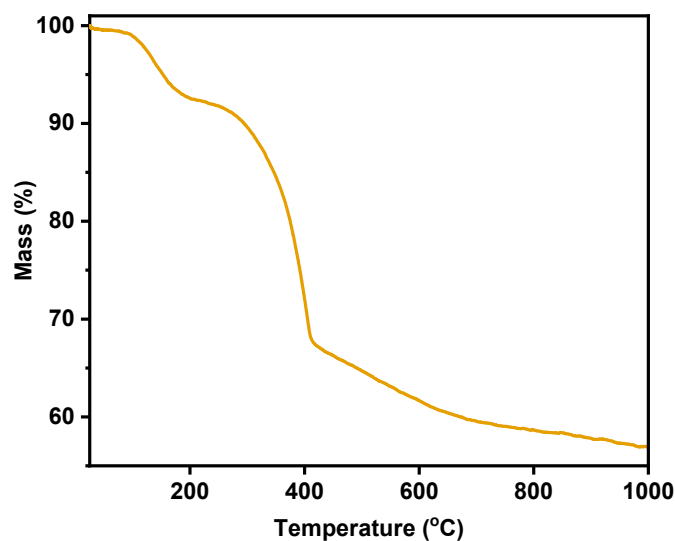
Fig. S12. TGA of Ind-CPP conducted in N$_2$ atmosphere at 10°C/min temperature increment rate.


**Fig. S13.** Deconvoluted C1s HR-XPS spectra of Ind-CPP.

Discussion S6: XPS

The high-resolution XPS pattern of the C1s region can be deconvoluted into 5 sub-apexes using the best-fitting scenario. The main peak with the highest density at 283.9 eV is ascribed to the aromatic sp^2 C=C and aromatic C-H. Apart from this, a secondary band centering at 284.9 eV originates from the sp C≡C. The higher bond order of the alkyne unit compared to aromatic C=C is deemed to be the reason behind this up-field binding energy peak. C–N and C–O appeared at 285.5 and 286.0 eV respectively, while the small satellite hump at 289.1 is ascribed to the π−π∗ transition in the aromatic network.

13

The CPP was pre-treated in a similar way as for solid-state NMR and FTIR described earlier to minimize the contribution of trapped solvents and air. However, a trivial contribution from aerial O_2 and moisture (H_2O) can be perceived in the HR-XPS spectrum of the O1s region (see Fig. 1g, main text). The inevitable air exposure of the polymer during its loading onto the XPS analyzer may have caused those peaks.
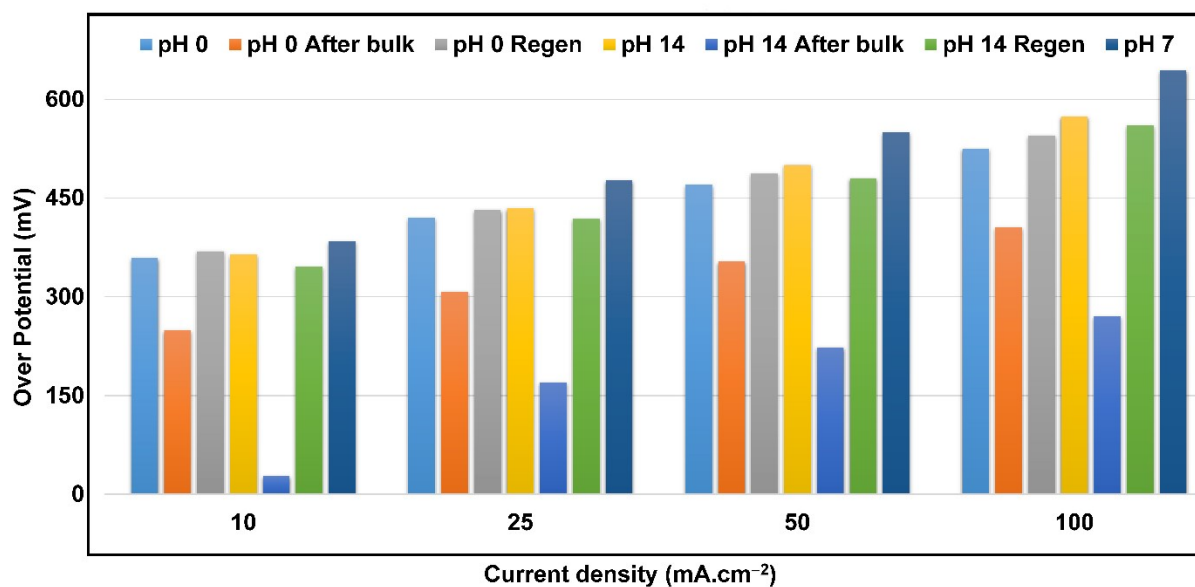
Fig. S14. Comparison of overpotentials at current density 10, 25, 50, and 100 mA/cm^2 by fresh Ind-CPP, Ind-CPP after bulk, and regenerated Ind-CPP at pH 0 and 14.
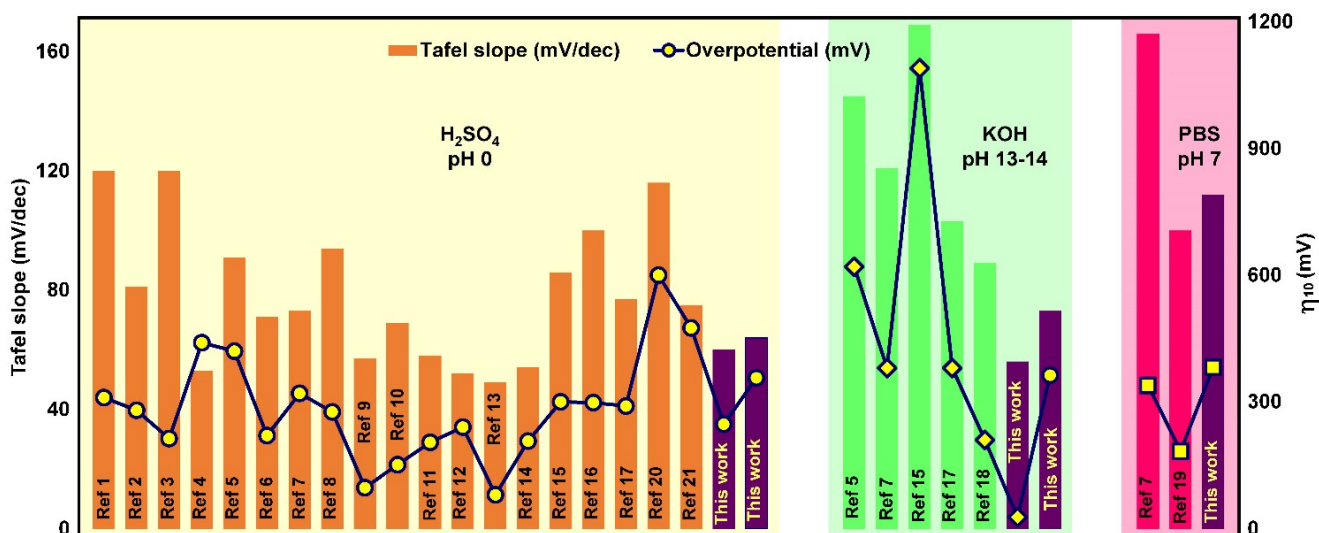
Fig. S15. Comparison of the catalytic activities (η_{10} and Tafel slope) for various metal-free catalysts under acidic (orange), alkaline (green), and neutral (pink) medium.

Discussion S7: Comparison of the catalytic activity of Ind-CPP with reported metal-free catalysts

The catalytic activity of Ind-CPP is compared with other state-of-the-art metal-free electrocatalysts reported to date for HER from water. Most of the material in this regime is comprised of carbonaceous matrices (e.g., graphene, CNT, Fullerene etc.), graphitic carbon nitride, their heteroatom substituted analogues, and/or composites, while examples of a relatively new genre of heterogeneous organic structures e.g., conjugated polymers/composites, covalent organic framework etc. manifesting similar activity are only a handful. More than 90% of these organic electrocatalysts are typically active in the acidic medium as the presence of excess H^+ favours H_2 generation. Organic matrices working under alkaline conditions are quite rare, whereas materials showing HER activity in the neutral medium are the rarest. Among these conditions, only one material comprised of CNT and C_{60} has been reported to date as a true pH-universal electrocatalyst maintaining its activity in acidic, alkaline, and neutral media. Our material, Ind-CPP, reported herein also falls in this true pH-universal category. A careful comparison of the η_{10} and Tafel slope values indicates that Ind-CPP manifests moderate activity in acidic water, with both kinetic parameters at par with other reported catalysts, while in an alkaline medium, it outpassed all other organic metal-free HER electrocatalysts *vis-à-vis* both η_{10} and Tafel slope. On the other hand, the catalytic results are far more promising in neutral medium. This comparative report offers a holistic picture of the metal-free organic HER matrices and justifies the superiority of our catalyst compared to others.

15

Table S2. Comparison of the material composition and catalytic activities (η_{10} and Tafel slope) for various metal-free catalysts under acidic, alkaline, and neutral medium (corresponding to Fig. S12 *vide supra*)[a]

Entry	Name	Material type	Medium	η_{10} (mV)	Tafel slope (mV/dec)	Ref
1	N,S-G	N and S co-doped graphene	0.5 M H$_2$SO$_4$	310	120	3
2	NS-500	N and S co-doped graphene	0.5 M H$_2$SO$_4$	280	81	4
3	NPG900	N and P co-doped graphene	0.5 M H$_2$SO$_4$	213	120	5
4	PS-rGO	S and P co-doped reduced graphene oxide	0.5 M H$_2$SO$_4$	440	53	6
5	N, P-G	N and P co-doped graphene	0.5 M H$_2$SO$_4$	420	91	7
			0.1 M KOH	620	145	
6	p-MWCNTs-ao-cp	Carbon nanotube	0.5 M H$_2$SO$_4$	220	71	8
7	C$_{60}$-SWCNT	Fullerene doped carbon nano tube	0.1 M KOH	380	121	9
			PBS pH 7	339	166	
			0.5 M H$_2$SO$_4$	320	73	
8	NDC-800	N doped carbon	1.0 M H$_2$SO$_4$	276	94	10
9	HPC-800	N and S co-doped porous carbon	0.5 M H$_2$SO$_4$	97	57	11
10	PANI-PA-900	N and P co-doped carbon from Phytic Acid	0.5 M H$_2$SO$_4$	151	69	12
11	SA900ZC	P, N and O co-doped Carbon	0.5 M H$_2$SO$_4$	204	58	13
12	C$_3$N$_4$@NG	N doped graphene @ carbon nitride	0.5 M H$_2$SO$_4$	240	52	14
13	PCN@N-graphene-750	carbon nitride @ N doped graphene	0.5 M H$_2$SO$_4$	80	49	15
14	g-C$_3$N$_4$ nanoribbon-G	carbon nitride and graphene	0.5 M H$_2$SO$_4$	207	54	16
15	g-C$_3$N$_4$@S-Se-pGr	carbon nitride @ S and Se co-doped graphene	0.5 M H$_2$SO$_4$	300	86	17
			0.1 M KOH	1090	169	
16	B$_x$C$_y$N$_z$	B-doped carbon nitride	0.5 M H$_2$SO$_4$	298	100	18
17	N,S-CN	N and S co-doped carbon	0.5 M H$_2$SO$_4$	290	77	19
			0.1 M KOH	380	103	

18	MPSA/GO-1000	N and P co-doped carbon/GO	0.1 M KOH	210	89	20
19	SiO$_2$/PPy NTs-CFs	Poly pyrrole nanotube on silica	PBS pH 7	183	100	21
20	PR-GDY	pyrazine-graphdiyne conjugated polymer	0.5 M H$_2$SO$_4$	475	75	22
			0.1 M NaHCO$_3$ + 0.1 M Na$_2$CO$_3$	710	275	
21	SB-PORPy COF	Porphyrin and pyrene-based covalent organic framework	0.5 M H$_2$SO$_4$	N.A.	116	23
22	**Ind-CPP**	**Indigo-based conjugated polymer**	**0.5 M H$_2$SO$_4$**	**359**	**64**	**This work**
			PBS pH 7	**384**	**112**	
			1 M KOH	**364**	**73**	
			0.5 M H$_2$SO$_4$ (after bulk)	**249**	**60**	
			1 M KOH (after bulk)	**28**	**56**	

[a] Most of the metal-free HER electrocatalysts reported to date were performed under acidic conditions. Only a handful of materials were active in alkaline or neutral medium (colour coated in green), whereas only one recent report has been found on a true pH-universal metal-free catalyst, *except ours* (colour coated in cyan).
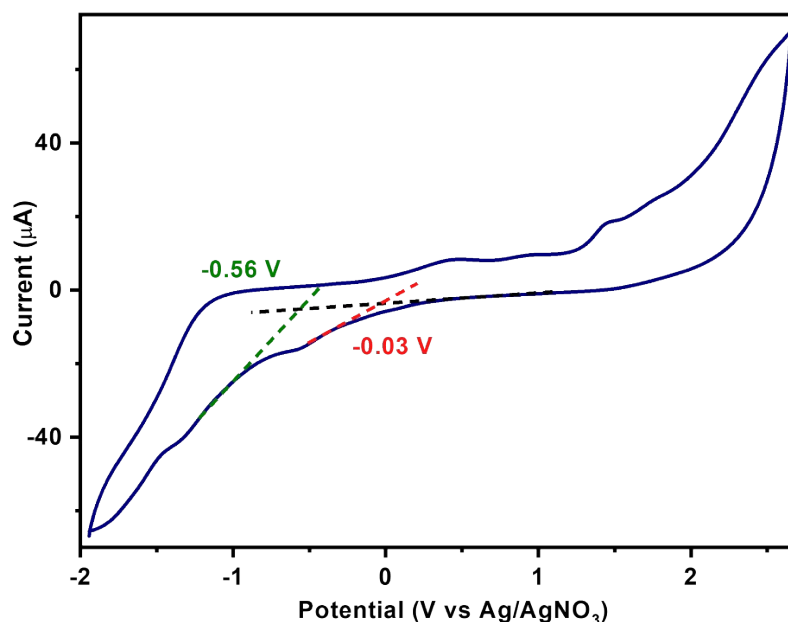
Fig. S16. The CV of Ind-CPP measured in acetonitrile shows two reduction peaks at -0.03 V and -0.56 V (*vs* Ag/AgNO$_3$).
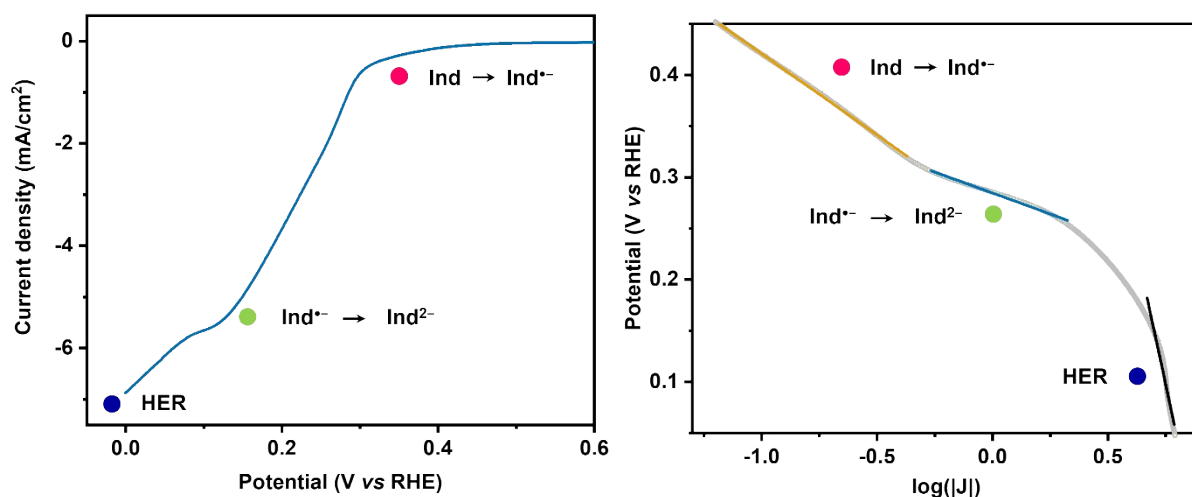
Fig. S17. LSV of Ind-CPP measured in aqueous PBS (pH 7) (left) and corresponding log(current density) vs potential curve (right) showing that Ind-CPP underwent stepwise two-electron reduction in water (i.e., from Ind to Ind$^{\bullet-}$ (pink dot) and then from Ind$^{\bullet-}$ to Ind^{2-} (green dot)) before it starts reducing water to H$_2$ (blue dot).
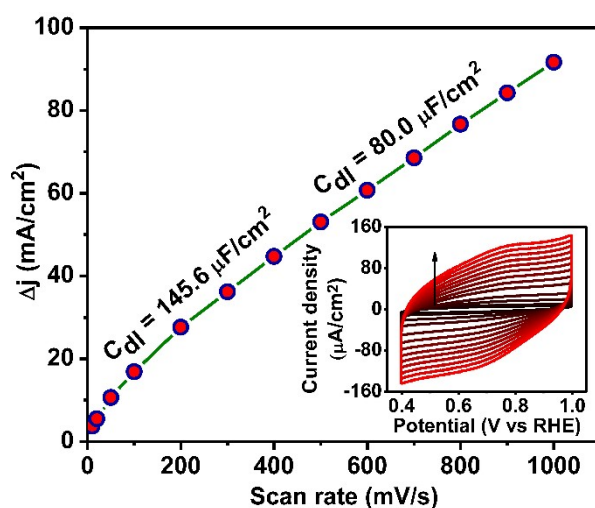
Fig. S18. The double-layer capacitance of Ind-CPP is calculated from the non-Faradic region of its cyclic voltammogram (inset).

Table S3. Elemental analysis (C, H, N, O) of Ind-CPP.

	C %	H %	N %	O %
Experimental	79.49	2.78	8.67	9.06
Calculated	80.44	2.81	7.82	8.63

Discussion S8: Calculation of electrochemically active surface area, HER turnover frequency, and amount of H$_2$ produced

ECSA calculation:

The electrochemical surface area (cm^2) can be calculated from the electrical double-layer capacitance C$_{dl}$ following the mathematical formula:

$$ECSA = \frac{C_{dl}}{10} = \frac{145.58}{10} cm^2 = 14.56 \; cm^2$$

Where capacitance for a standard glassy carbon electrode is considered 10 µF/cm^2.

Since the electrochemical HER activities were measured at a low scan rate (10 mV/s), 145.58 C$_{dl}$ is considered for Ind-CPP.

TOF for H$_2$ production:

The TOF can be calculated following the below formula:

$$TOF = \frac{Number \; of \; H_2 \; turnovers \; per \; cm^2 \; ECSA}{Number \; of \; active \; sites \; per \; cm^2 \; geometrical \; area}$$

Total H$_2$ turnover per unit cm^2 geometrical area can be calculated from the current density following the equation:

$$No. \; of \; H_2 = \left(j\frac{mA}{cm^2}\right)\left(\frac{1 \; C/s}{1000 \; mA}\right)\left(\frac{1 \; mol \; of \; e^-}{96485.3 \; C}\right)\left(\frac{1 \; mol \; of \; H_2}{2 \; mol \; of \; e^-}\right)\left(\frac{6.022 \; \times \; 10^{23} \; H_2 \; molecules}{1 \; mol \; H_2}\right)$$

$$= (3.12 \times 10^{15} \times j) \; No. \; of \; H_2$$

We reckon that in our case the indigo units or better put the bay positions of the indigo core, acted as the active sites for H$_2$ production. Therefore, it is justifiable to calculate the number of indigo cores present in the unit geometrical electrode area as a quantifiable alternative to the active sites.

The elemental analysis given in Table S2 conferred the similarity of the experimental and theoretically predicted model of Ind-CPP (as given in Fig. S2). The molecular weight of this model can be calculated as 358.35 g/mol.

Considering that the only source of N-atom in the polymer is indigo, the amount of indigo functionality present per mol of the CPP can be quantified from the elemental analysis report. Theoretically, 7.82% N-content infers 1 mol of indigo per mol CPP. Therefore, the experimental 8.67% N-content would account for 1.109 mol of indigo per mol of CPP. As indicated in the electrode preparation method, a 500 µL homogeneously dispersed ink containing 2 mg CPP material was obtained and 10 µL of that ink was drop cast on the electrode featuring a geometrical surface area of 0.07 cm^2.

Therefore, the mol of indigo units present per cm^2 electrode surface can be given by,

$$mol \; of \; Indigo = \left(\frac{amount \; of \; CPP \; in \; the \; dropcasted \; ink}{geometrical \; surface \; area \; of \; the \; electrode}\right) \times \left(\frac{mol \; of \; Indigo \; unit}{weight \; of \; 1 \; mmol \; CPP}\right) \times 1cm^2$$

$$= \left(\frac{2mg \times 10\mu L/500\mu L}{0.07\ cm^2}\right) \times \left(\frac{1.109\ mol}{358.35\ mg}\right) \times 1cm^2 = 1768.33 \times 10^{-6}\ mol = 1064.89 \times 10^{15}\ counts$$

Since the indigo moiety contains two-bay positions, we can assume that each indigo is responsible for 2 molecules of H_2 production at a time. Therefore, the expression of TOF for our catalyst can be rearranged as:

$$TOF = \left(\frac{3.12 \times 10^{15} \times 14.56}{2 \times 1064.89 \times 10^{15}}\right) \times j\ No.\ of\ H_2\ per\ sec$$

$$= (0.02133 \times j)\ H_2/s$$

Considering the metal-free nature of the material, such high TOF confer substantial HER activity of Ind-CPP.

The calculation for the amounts of H_2 produced:

Considering the most active condition of Ind-CPP (i.e., after bulk electrolysis at pH 14) at 250 mV overpotential:

H_2 production $= 1.58\ molecules\ per\ catalytic\ site\ in\ each\ sec.$

Hence, 1 mol Ind-CPP that contains 2 mol active sites (two-bay positions of indigo) each producing 1.58 mol H_2/s will generate a total of $(2 \times 1.58 \times 3600) = 11376\ mol\ H_2/h$

Or each 1g of Ind-CPP will produce $(11376/358.35) = 31.75\ mol\ H_2/h$ [Since M.W. of the material is 358.35]

1 mol of gas corresponds to 22.4 L, and density of H_2 is 0.08988 g/L

Hence, 1 g of Ind-CPP will produce $= (31.75 \times 22.4 \times 0.08988 \times 24/1000)\ kg/day = 1.53\ kg/day$
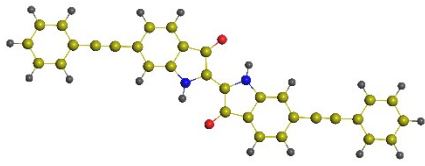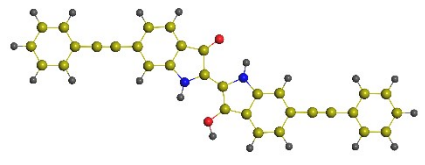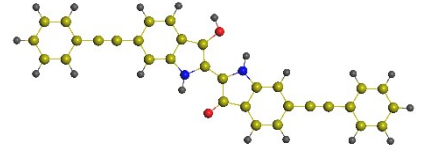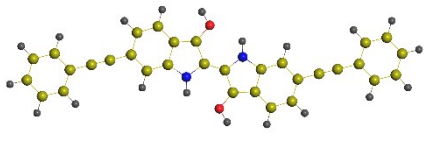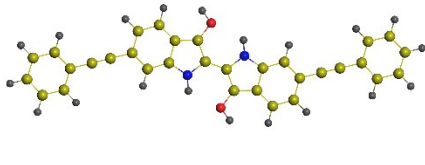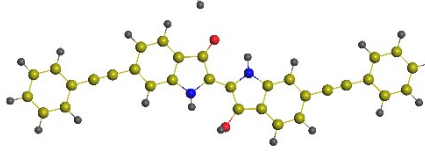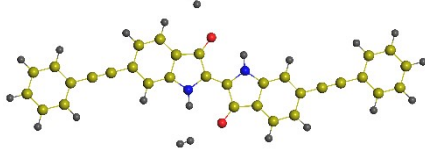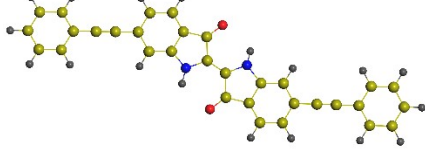
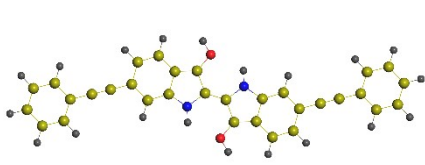i.e., only 1 gram of the metal-free material can produce 1.53 kg of H_2 gas per day.
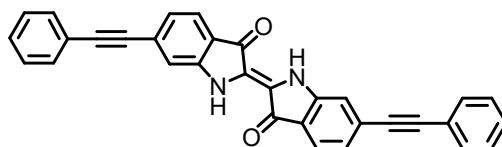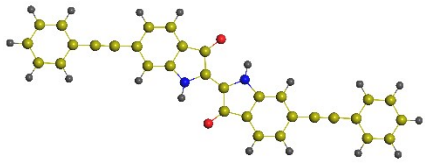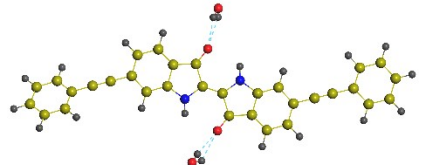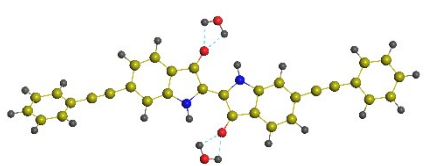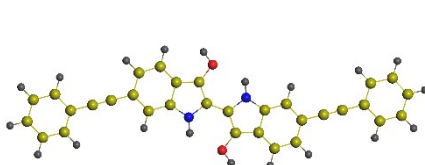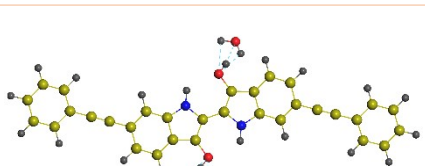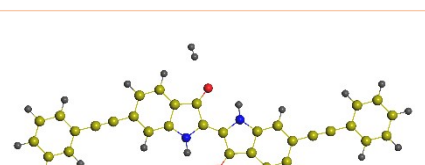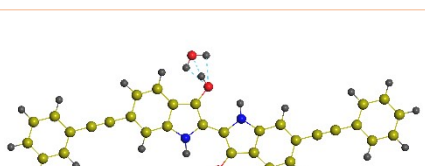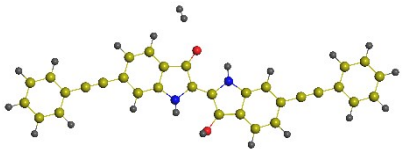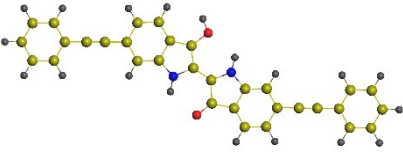
***Fig.* S19.** Chemical structure of Ind-Mod, the model analogue of Ind-CPP.

Table S4. The structures of the active catalytic units for HER under acidic, neutral, and alkaline medium with theoretically computed Enthalpy of Formation, Heat Capacity and Entropy.
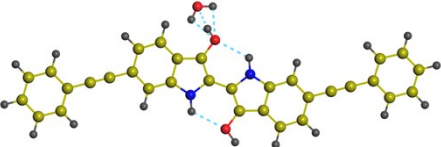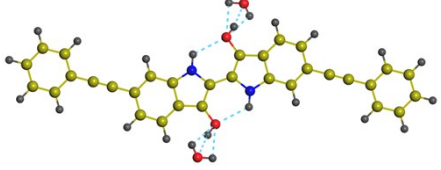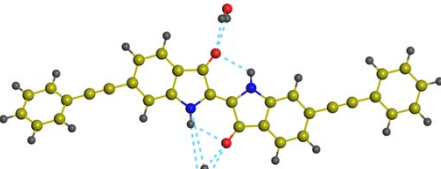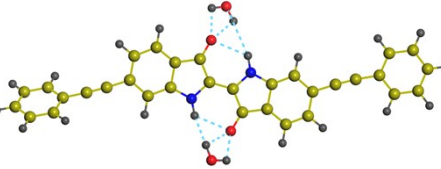
Entry	Name	Structure	Enthalpy of Formation (cal/mol)	Heat Capacity (cal/mol)	Entropy (cal/mol)	Free energy at RT (eV)
1	A1		18051.7660	109.9388	193.4643	-1.7170

2	A2		18248.7415	111.3826	193.6152	-1.7104
3	A2'		18149.2611	111.2362	193.0464	-1.7074
4	A3		18219.4937	112.0772	185.5396	-1.6074
5	A3'		18509.8459	113.3882	193.6417	-1.6994
6	A4		19032.4431	114.5225	200.7340	-1.7684
7	A5		20296.4464	121.0233	210.2338	-1.8363
8	A6		22011.6385	129.5280	224.0681	-1.9407
9	B1		18051.7660	109.9388	193.4643	-1.7170

10	B2		18248.7415	111.3826	193.6152	-1.7104
11	B2'		23055.4550	131.7427	241.6911	-2.1232
12	B3		22798.3837	131.3279	244.8445	-2.1750
13	B3'		18509.8459	113.3882	193.6417	-1.6994
14	B4		19032.4431	114.5225	200.7340	-1.7684
15	B5		23128.1610	134.5083	236.4501	-2.0523
16	B6		20296.4464	121.0233	210.2338	-1.8363
17	B7		21053.7346	124.5045	218.7520	-1.9136

		Molecule			
18	B8		20378.8655	120.8086	211.3829	-1.8476
19	B9		18219.4937	112.0772	185.5396	-1.6074

Table S5. The structures, H-bonding interaction and the formation energy for water-associated Ind-CPP intermediates.

Molecule	Name	Bay H-bond length (Å)	Ind-H_2O H-bond length (Å)	Free energy (eV)
	B7	2.293 2.295	2.424 2.178 2.404	-1.9136
	B5	2.297 2.501	2.445 2.167 2.410 2.419 2.163 2.449	-2.0523
	B2'	2.370 2.386	2.236 2.256 2.225 2.221 3.234 3.717	-2.1232
	B3	2.319 2.282	2.091 2.135 3.553 2.140 2.068 3.204	-2.1750

Reference:

1. Truger, M., Roscioni, O. M., Röthel, C., Kriegner, D., Simbrunner, C., Ahmed, R., Głowacki, E. D., Simbrunner, J., Salzmann, I., Coclite, A. M., Jones, A. O. F., and Resel, R. (2016). Surface-induced phase of Tyrian Purple (6,6′-Dibromoindigo): thin film formation and stability. *Cryst. Growth Des. 16*, 3647-3655.

2. Kim, J., Kwon, S., Cho, D.-H., Kang, B., Kwon, H., Kim, Y., Park, S. O., Jung, G. Y., Shin, E., Kim, W.-G., Lee, H., Ryu, G. H., Choi, M., Kim, T. H., Oh, J., Park, S., Kwak, S. K., Yoon, S. W., Byun, D., Lee, Z., and Lee, C. (2015). Direct exfoliation and dispersion of two-dimensional materials in pure water via temperature control. *Nat. Commun. 6*, 8294.

3. Jiao, Y., Zheng, Y., Davey, K., and Qiao, S.-Z. (2016). Activity origin and catalyst design principles for electrocatalytic hydrogen evolution on heteroatom-doped graphene. *Nat. Energy 1*, 16130.

4. Ito, Y., Cong, W., Fujita, T., Tang, Z., and Chen, M. (2015). High catalytic activity of nitrogen and sulfur Co-doped nanoporous graphene in the hydrogen evolution reaction. *Angew. Chem. Int. Ed. 54*, 2131-2136.

5. Jiang, H., Zhu, Y., Su, Y., Yao, Y., Liu, Y., Yang, X., and Li, C. (2015). Highly dual-doped multilayer nanoporous graphene: efficient metal-free electrocatalysts for the hydrogen evolution reaction. *J. Mater. Chem. A 3*, 12642-12645.

6. Khalid, M., and Varela, H. (2018). A general potentiodynamic approach for red phosphorus and sulfur nanodot incorporation on reduced graphene oxide sheets: metal-free and binder-free electrodes for supercapacitor and hydrogen evolution activities. *J. Mater. Chem. A 6*, 3141-3150.

7. Zheng, Y., Jiao, Y., Li, L. H., Xing, T., Chen, Y., Jaroniec, M., and Qiao, S. Z. (2014). Toward design of synergistically active carbon-based catalysts for electrocatalytic hydrogen evolution. *ACS Nano 8*, 5290-5296.

8. Cui, W., Liu, Q., Cheng, N., Asiri, A. M., and Sun, X. (2014). Activated carbon nanotubes: a highly-active metal-free electrocatalyst for hydrogen evolution reaction. *Chem. Commun. 50*, 9340-9342.

9. Gao, R., Dai, Q., Du, F., Yan, D., and Dai, L. (2019). C_{60}-adsorbed single-walled carbon nanotubes as metal-free, pH-universal, and multifunctional catalysts for oxygen reduction, oxygen evolution, and hydrogen evolution. *J. Am. Chem. Soc. 141*, 11658-11666.

10. Singh, D. K., Jenjeti, R. N., Sampath, S., and Eswaramoorthy, M. (2017). Two in one: N-doped tubular carbon nanostructure as an efficient metal-free dual electrocatalyst for hydrogen evolution and oxygen reduction reactions. *J. Mater. Chem. A 5*, 6025-6031.

11. Liu, X., Zhou, W., Yang, L., Li, L., Zhang, Z., Ke, Y., and Chen, S. (2015). Nitrogen and sulfur co-doped porous carbon derived from human hair as highly efficient metal-free electrocatalysts for hydrogen evolution reactions. *J. Mater. Chem. A 3*, 8840-8846.

12. Yan, D., Dou, S., Tao, L., Liu, Z., Liu, Z., Huo, J., and Wang, S. (2016). Electropolymerized supermolecule derived N, P co-doped carbon nanofiber networks as a highly efficient metal-free electrocatalyst for the hydrogen evolution reaction. *J. Mater. Chem. A 4*, 13726-13730.

13. Wei, L., Karahan, H. E., Goh, K., Jiang, W., Yu, D., Birer, Ö., Jiang, R., and Chen, Y. (2015). A high-performance metal-free hydrogen-evolution reaction electrocatalyst from bacterium derived carbon. *J. Mater. Chem. A 3*, 7210-7214.

14. Zheng, Y., Jiao, Y., Zhu, Y., Li, L. H., Han, Y., Chen, Y., Du, A., Jaroniec, M., and Qia, S. Z. (2014). Hydrogen evolution by a metal-free electrocatalysts. *Nat. Commun*. *5*, 3783.

15. Duan, J., Chen, S., Jaroniec, M., and Qiao, S. Z. (2015). Porous C_3N_4 Nanolayers@N-Graphene films as catalyst electrodes for highly efficient hydrogen evolution. *ACS Nano 9*, 931-940.

16. Zhao, Y., Zhao, F., Wang, X., Xu, C., Zhang, Z., Shi, G., and Qu, L. (2014). Graphitic carbon nitride nanoribbons: graphene-assisted formation and synergic function for highly efficient hydrogen evolution. *Angew. Chem. Int. Ed*. *53*, 13934-13939.

17. Shinde, S. S., Sami, A., and Lee, J.-H. (2015). Electrocatalytic hydrogen evolution using graphitic carbon nitride coupled with nanoporous graphene co-doped by S and Se. *J. Mater. Chem. A 3*, 12810-12819.

18. Chhetri, M., Maitra, S., Chakraborty, H., Waghmare, U. V., and Rao, C. N. R. (2016). Superior performance of borocarbonitrides, $B_xC_yN_z$, as stable, low-cost metal-free electrocatalysts for the hydrogen evolution reaction. *Energy Environ. Sci*. *9*, 95-101.

19. Qu, K., Zheng, Y, Zhang, X., Davey, K., Dai, S., and Qiao, S. Z. (2017). Promotion of electrocatalytic hydrogen evolution reaction on nitrogen-doped carbon nanosheets with secondary heteroatoms. *ACS Nano 11*, 7293-7300.

20. Zhang, J., Qu, L., Shi, G., Liu, J., Chen, J., and Dai, L. (2016). N,P-Codoped carbon networks as efficient metal-free bifunctional catalysts for oxygen reduction and hydrogen evolution reactions. *Angew. Chem. Int. Ed. 55*, 2230-2234.

21. Feng, J.-X., Xu, H., Ye, S.-H., Ouyang, G., Tong, Y.-X., and Li, G.-R. (2017). Silica-polypyrrole hybrids as high-performance metal-free electrocatalysts for the hydrogen evolution reaction in neutral media. *Angew. Chem. Int. Ed*. *56*, 8120-8124.

22. Sakamoto, R., Shiotsuki, R., Wada, K., Fukui, N., Maeda, H., Komeda, J., Sekine, R., Harano, K., and Nishihara, H. (2018). A pyrazine-incorporated graphdiyne nanofilm as a metal-free electrocatalyst for the hydrogen evolution reaction. *J. Mater. Chem. A 6*, 22189-22194.

23. Bhunia, S., Das, S. K., Jana, R., Peter, S. C., Bhattacharya, S., Addicoat, M., Bhaumik, A., and Pradhan, A. (2017). Electrochemical stimuli-driven facile metal-free hydrogen evolution from pyrene-porphyrin-based crystalline covalent organic framework. *ACS Appl. Mater. Interfaces 9*, 23843-23851.